Porosity Characterization of High-pressure die-cast Plates by a Fusion of Ultrasonic and X-ray Measuring Methods and Explainable Data-driven Modeling

Stefan Bosse[1], Jens Prager[3], Dirk Gohlke[3], Dirk Lehmhus[2]
[1]University of Koblenz, Dept. of Computer Science, Koblenz, Germany
[2]Fraunhofer IFAM, Bremen, Germany
[3]Bundesanstalt für Materialforschung und -prüfung (BAM), Berlin, Germany

Abstract. This study investigates various measuring techniques for identifying and characterizing defects, particularly pores, in thin-walled high-pressure die-cast (HPDC) aluminum samples with differing alloy compositions. It focuses on non-destructive testing methods like X-ray radioscopy and different Ultrasonic testing approaches. The samples represent the AlSi10MnMg alloys, with variations in secondary material content. The research classifies porosity into four classes based on size, distribution, and density, using sensor data for Automated Defect Recognition (ADR). Results indicate that Ultrasonic wave responses help classify alloy compositions and porosity classes, revealing correlations between HF Ultrasonic signals and material features. Additionally, X-ray and Ultrasonic immersion techniques are used to collect reference data. The study also suggests limited effectiveness of Machine Learning models for defect prediction but emphasizes its importance for improving aluminum casting quality, particularly towards sustainable materials.
Keywords: Non-destructive Testing; Ultrasonic Monitoring; Pores; Alloys, Machine Learning; High-pressure Die casting

1. Introduction

The growing use of aluminum in the automotive industry contributes to the fact that secondary aluminum is scarce, and cannot easily be sourced from other industries, as they tend to have their recycling chains and networks already in place. Besides, the demand in terms of alloys for structural parts does not match what is on offer from powertrain components: Available materials tend to have e.g. higher content levels of elements like copper, iron, zinc or manganese. As a consequence, there is a considerable body of literature by now which focuses on analyzing the impact of such accumulations on material characteristics like castability, mechanical strength or corrosion resistance [1,2,3]. The present paper adds another perspective: We compare a primary alloy with two nominally similar alloys featuring different levels of secondary material content – however, we do not only look at composition, but also at defects: Do these come out differently in primary and secondary alloys, and do they affect mechanical characteristics differently? We base these evaluations on inspection of X-ray radioscopy images of samples to identify four different quality level classes, an Automated Defect Recognition (ADR) approach applied to a more detailed set of radioscopy images introduced in earlier work by Bosse et al. [4], and high-frequency Ultrasonic testing results to enable fast quality classification.

This study explores the fusion of different measuring methods to identify, classify, and characterize defects (pores) in thin-walled high-pressure die-cast (HPDC) aluminum samples. We focus on non-destructive testing (NDT) techniques such as X-ray radioscopy and a fusion of different Ultrasonic testing (UT) methods, i.e., contact-based pulse-echo high-frequency (HF) Us (A- and B-scan), mainly using low-cost transducers, as well as high-quality scanning immersion techniques (C-scan). The sample set consists of three different alloy compositions with a broad range of porosity, split in four different porosity classes classified with respect to pore size, pore distribution, and pore density. Previous X-ray μCT and radioscopy analysis ([4]) showed pore size ranges from the μm to the mm scales.

To assess specimens we need different quantitative and qualitative measures. The porosity analysis is central. Wilczek et al. [5] compared different measuring methods to assess the porosity of die casted specimens. They conclude that X-ray Computed Tomography (CT) and radioscopy are suitable methods to get an accurate measure of the porosity, but outline the limited usability of Ultrasonic testing (UT). But X-ray testing is expensive and not well suited for in-field diagnostics, in contrast to Ultrasonic measuring techniques, e.g., pulse-echo measurements with one transducer, as used by Boichuk et al. [6] to assess the porosity of polymer composite materials. Hillger et al. [7] as well as Adler et al. [8] also showed porosity assessment by the frequency spectrum of the UT response signal for die casted specimens with controlled porosity contents ranging from 0% to 6%. The frequency of the stimulus signal as well as the main center frequency of transducer are reported in the 1-10 MHz range. Early work from Gubernatis and Domany [9] and by Rose [10] formulated a theoretical approach for the interaction of Ultrasonic waves in porous materials. They found a relationship of the frequency-dependent elastic wave attenuation with the porosity of the material. For wavelength much larger than the pore size, the attenuation is proportional to the third power of the frequency, whereas if the wavelength is smaller than the pore size the attenuation is not dependent on the frequency. The exact dependency is not relevant for us because we want only to perform porosity classification.

Based on this works, we assume that a suitable signal feature for aggregated porosity classification is the frequency spectra from multi-resonance or broadband transducers (and short pulse excitation). But we found that the frequency spectrum distribution can be used to classify the alloy composition, too. In contrast to work by [8] assuming a homogeneous pore distribution (with respect to size and spatial distribution) we found inhomogeneous spatial distribution, which makes the pore assessment more challenging.

We will show the limited use of Machine Learning models for the prediction of defects from reduced sensor data, in image processing and automated porosity analysis applied to X-ray radioscopy images as well as porosity classification using Ultrasonic signals. The research has significance for advancing quality in aluminum casting, especially shifting towards sustainable materials with higher secondary content, which may influence defect formation and mechanical performance. The results show varying strong and weak correlation between HF Ultrasonic signals and the detectable material features (alloy composition and porosity). Data-driven models can help to map weak signal features on these material features, but as demonstrated in this work with a low degree of generalization. X-ray radioscopy as well as very high frequency scanning Ultrasonic immersion methods are used here only as reference methods for the initial material characterization and data labeling (experimentally estimated ground truth).

2. Materials

Three different alloys were compared in this study, all of them conforming to the specification of an AlSi10MnMg casting alloy in accordance with the alloy designation EN AC-43500, DIN EN 1706:2021-10 [12]. One of these alloys was entirely based on primary materials (Silafont-36®, Aluminium Rheinfelden Alloys GmbH, Rheinfelden, Germany), while two others contained 58 wt.-% (Aluminium Rheinfelden Alloys GmbH, Rheinfelden, Germany) and 89 wt.-% (SILVAL 10®, Raffmetal S.p.a., Casto, Italy) of secondary aluminum. The exact composition of these alloys in the as received state is given in Table 1. Prior to casting, Mg and Sr content levels were adjusted to approximately 0.27 wt.-% and 0.023 wt.-%, respectively, in all alloys to improve comparability. The HPDC die used for samples production is shown in Fig. 1.

Alloy	Element content level [wt.-%]														
	Si	Fe	Cu	Mn	Mg	Cr	Zn	Ti	Sr	Ni	Pb	Sn	Sb	Ca	P
Silafont-36® specification*	9.5-11.5	<0.15	<0.03	0.5-0.8	0.1-0.5	-	<0.07	0.04-0.15	0.010-0.025	-	-	-	-	-	<0.001
Silafont-36® 100 wt.-% primary**	10.28	0.082	0.002	0.513	0.146	0.001	0.001	0.008	0.002	-	-	-	-	-	-
AlSi10MnMg 58 wt.-% secondary**	10.18	0.13	0.02	0.61	0.27	0	0.01	0.06	0.0171	0.009	0.002	0.0006	0.002	-	-
SILVAL 10® Specification*	9.5-11	<0.35	<0.05	0.35-0.6	0.25-0.35	<0.03	<0.1	0.05-0.15	0.015-0.025	<0.05	<0.05	<0.05	<0.002	<0.002	<0.002
SILVAL 10® 89 wt.-% secondary**	9.95	0.338	0.023	0.471	0.279	0.011	0.026	0.075	0.0275	0.007	0.005	0.001	0	0.0009	0.001

* Supplier's specification. For Silafont-36®, maximum amount of elements for which no explicit limit is given is 0.10 wt.-%. For SILVAl 10®, the respective value is 0.15 wt.-%, which no individual element surpassing a threshold of 0.05 wt.-%.
** Supplier's analysis of the actual batches used in the present experiments.

Tab. 1. Composition of the alloys compared in the experiments: Supplier specifications and analyses of the actual batches used in the experiments as provided by the suppliers.

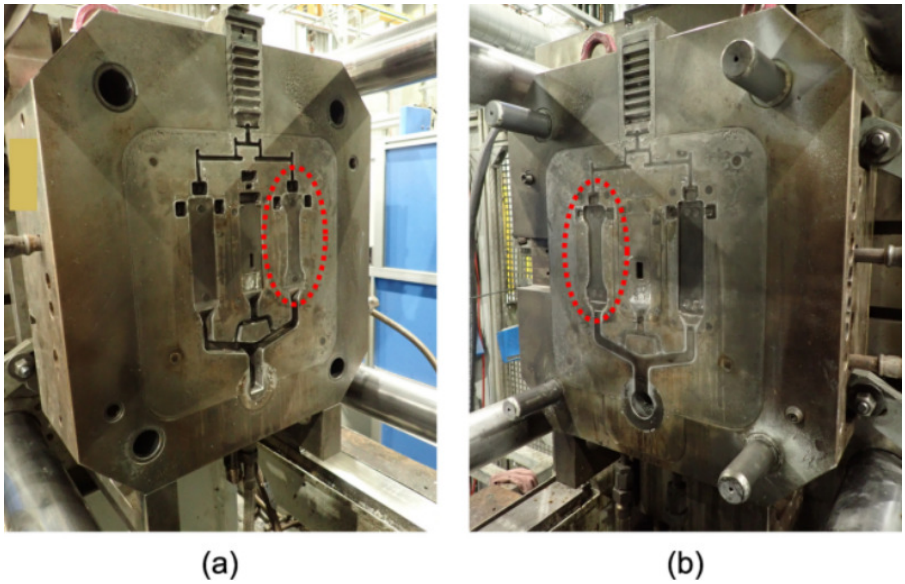

Fig. 1. HPDC die used for samples production: (a) movable side and (b) fixed side. The cavity from which the samples used in the present study is highlighted in red.

We distinguish four specimen classes (see Fig. 2 for examples):

A. First grade plates without detectable pores or only a very low fraction of small pores;

B. Second grade plates with a small amount of small or medium size pores;

C. Third grade plates with a significant amount of small and medium pores with a small amount of large pores;

D. Fourth grade plates with a lerge amount of pores including pore clusters and large pores (> 1 mm diameter).

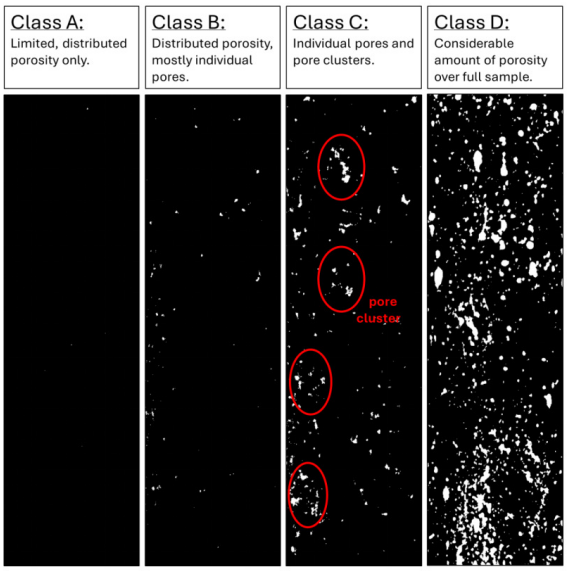

Fig. 2. Exemplary depiction of binarized X-ray images representing the four quality classes A, B, C and D (rejects) distinguished in visual inspection.

3. Methods

To assess specimens we need different quantitative and qualitative measures. We distinguish between primary and secondary measuring methods:

1. Primary measuring method: Pulse-echo UT investigated in this work to enable fast and low-cost aggregated porosity classification.
2. Secondary measuring methods: X-ray radioscopy and two-dimensional scanned immersion UT to enable detailed spatially resolved porosity assessment as reference data for 1.

In all measurements the specimens are scanned orthogonal to the plate surface (cross-section view) along the x- and y-axis for two-dimensional scanning and x-axis for single transducer measurements, as shown in Fig. 3. The UT measurement is performed at five positions.

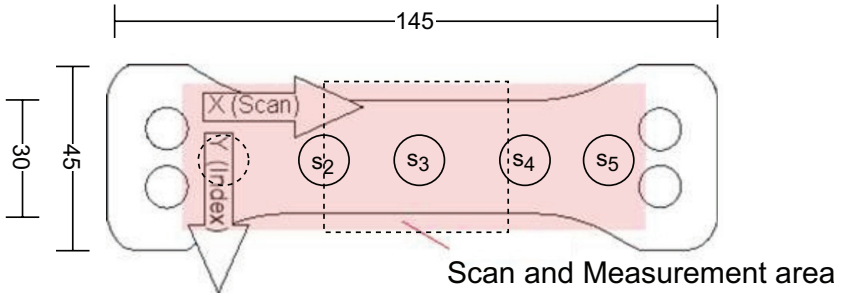

Fig. 3. The specimen geometry and the measuring paths (all dimensions in mm, thickness of plate is 3 mm). The *s* circles specify the pulse-echo UT positions, the dotted rectangular area denotes one X-ray image segment (4 overlapping segments in total along the x-axis).

3.1 X-ray Diagnostics

The X-ray diagnostics is used here for initial defect characterization. The results are used to investigate the Ultrasonic-based NDT methods as a ground data base.

Two measuring techniques are used:

1. X-ray radioscopy with µ focus X-ray tubes providing a 2-dim projection defects with full plate surface view and inspection (typically tiled in segments);
2. X-ray Computed Tomography (CT) provides a 3-dim ground characterization of defects like pores from a limited sample volume (not addressed in this work).

X-ray methods can only be used to detect and characterize defects based on material density variations. Other defects like oxide films cannot be detected.

The X-ray radioscopy images are used to provide statistical features of pores, as shown in Fig. 4:

1. Statistical measures of pore size (average, minimum and maximum, median, standard deviation);
2. Pore density;
3. Spatial pore distribution (mass of center);
4. Pore shape and orientation.

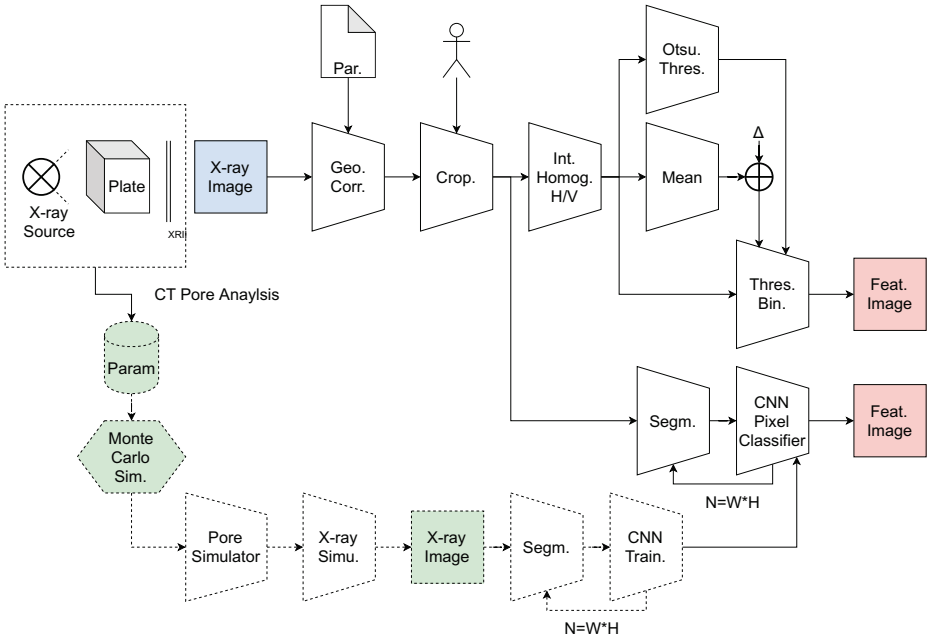

Fig. 4. Data flow and processing pipeline (with different branches) of the reference pore assessment and characterization using X-ray radioscopy images. X-ray CT is only used for a base set of pore statistics from few selected samples. X-ray radioscopy is applied to all samples. The ML model is trained with synthetic data from X-ray simulation (Derails can be found in [4]).

In previous work [4] we applied the radioscopy workflow to X-ray images acquired with a industrial X-ray machine equipped with a common tube focal spot diameter in the 200 µm range and a solid-state flat panel detector capturing the entire specimen (FOV 150 mm × 150 mm with 1024 × 1024 pixels, with a theoretical pixel resolution of 150 µm). In this work we used a µ-focus X-ray tube (Oxford Instrument) and an X-ray image intensifier (XRII) from Toshiba () capturing segments of the specimen (FOV 30 mm × 30 mm with a theoretical pixel resolution of 30 µm). This acquisition systems offers higher resolution but with increased noise and geometric distortions, which must be adjusted by geometric image transformations.

We compare two different methods for the pore identification and marking in X-ray radioscopy images:

1. Model-based: Image intensity homogenization using horizontal and vertical intensity integral vectors, followed by a threshold binarization (a) by using the mean intensity with an additional constant margin, and (b) by using the Otsu method determining the (global) threshold.

2. Model-free: A CNN ML model is used to mark pore areas in the X-ray image. The ML model is trained with synthetic data from X-ray simulation (as introduced in [4]).

The image processing computes a feature mark map image, as shown in Alg. 3. The original X-ray images have typically a non-uniform intensity profile along the horizontal and vertical axis (or any other orientation). For threshold binarization it is important to homogenize this non-uniform intensity profile, which is done in the function *PreProcessImage*. The marked pixels are collected as a pixel coordinate list, passed to a clusterer algorithm (DBSCAN), which returns a list of pixel groups belonging each to one pore (see [4] for details). The cluster list is finally processed to compute the pore area (and size) statistics, and optionally by an ellipse fitter providing relevant geometric measures for each pore (size, orientation).

3.2 Ultrasonic Diagnostics

3.2.1 Pulse-Echo

The main UT method used in this work for fast aggregate assessment of porosity bases on pulse-echo measurements with a two-crystal transducer attached to the surface via a coupling fluid, as shown in Fig. 5. The first transducer is used to inject a HF pulse wave into the cross section of the plate. The second transducer is used to record the delayed signal response capturing the reflected signal from the bottom side of the plate. The forward and backward wave propagation interact with pores and change the received signal.

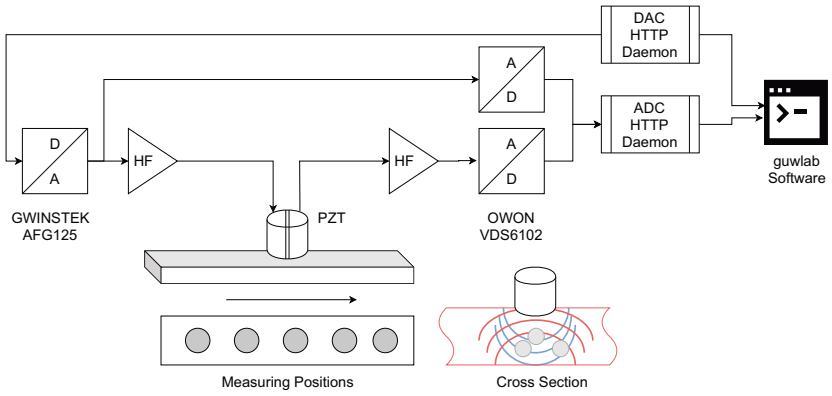

Fig. 5. Pulse-echo UT

3.2.2 Frequency Spectrum Analysis

The frequency spectrum contains multiple discrete resonance peaks, as shown in Fig. 6. It is assumed that each peak has an approximated Gaussian form. The measured signal response is spectrally analyzed by using FFT and Gaussian function regression (function fitting) to approximate the height, width, and center frequency of the resonance peaks. The frequency spectrum peaks are the feature attributes for the following pore and alloy analysis. Alg. 4 shows the basic algorithm for finding and characterizing peaks automatically, basically applying a smoothing function to the

spectrum and finding peaks by using the first and second derivative of the spectrum. Candidate peaks are fitted by using a parabolic approximation combined with a Gaussian function.

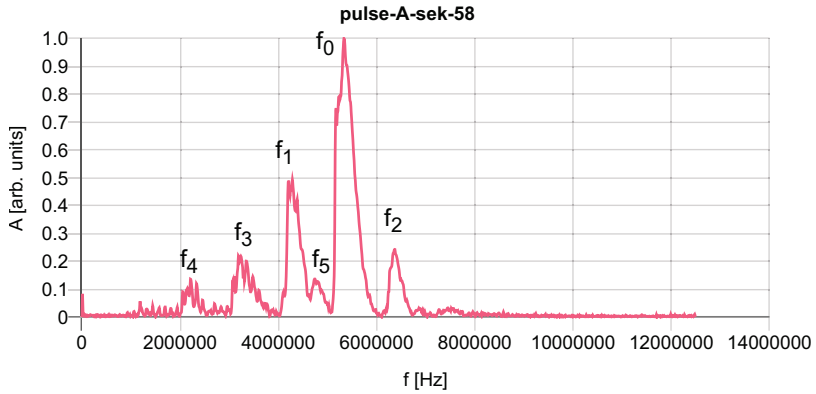

Fig. 6. An example of a frequency spectrum derived from the HF pulse-echo signal and the identification of the six relevant peaks. The primary main frequency is f_0, the secondary frequencies are f_1 and f_2, and the remaining peaks are third-level peals.

3.2.3 Scanned Immersion UT

This method is used to get another spatially resolved depth scan of the specimens. In contrast to X-ray inspection, UT can capture the detection of a wider range of defects including oxide films, which can be expected in die-casting processes. The specimen is placed here in water together with a focused HF transducer measuring in a pulse-echo configuration, too. The transducer can be moved in two spatial directions with a scanning raster in the mm range.

4. Experiments

4.1 X-ray Pore Analysis

The X-ray images were used to provide a reference classification of the specimens (labels for the UT-based classification). An example is shown in Fig. 7. The summary of the pore analysis for all specimens (and image segments) is shown in Fig. 8, as well as the results of a clustering of specimens using supervised learning with a Self-organizing Map (SOM) with selected pore features. The pore statistics shows a broad range of pore sizes and pore density. The SOM clustering shows a suitable separation of specimens using the two leading attributes "number of pores per mm^2" and "relative pore density". The average pore size is about 0.5 mm (mean diameter), the average density is about 0.3%.

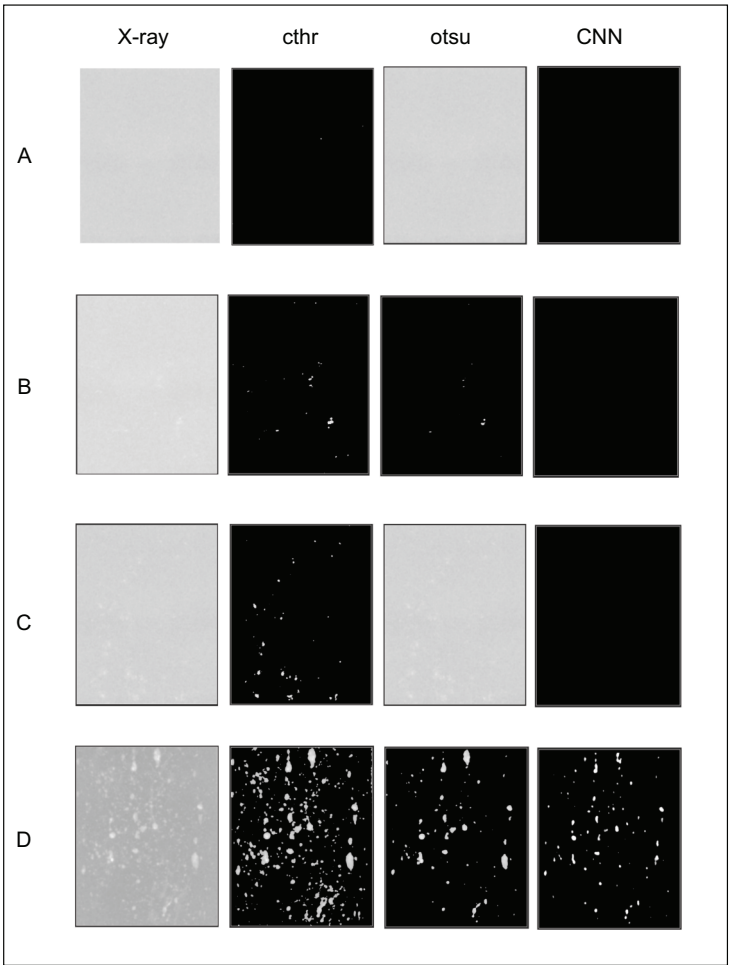

Fig. 7. Comparison of X-ray images, constant and otsu threshold binarization as well CNN-ML pore feature marking.

Fig. 8 shows examples of pore feature marking from X-ray images using the constant threshold method, the otsu method, and the ML CNN pixel classifier. The simplest constant threshold method, i.e., threshold is mean intensity + fixed Δ, outperforms all other methods. In contrast to previous work, where the CNN pixel classifier was applied to X-ray images from a standard X-ray imaging system, the pore feature marking fails here, except for class D specimens.

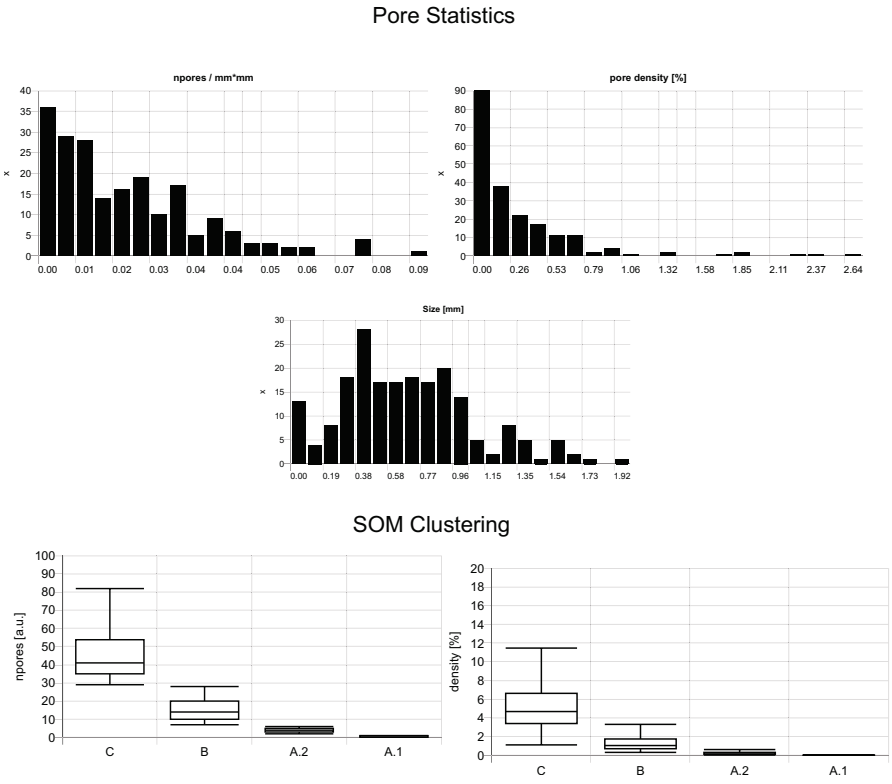

Fig. 8. (Top) Pore statistics computed from X-ray images for all specimens and all image segments (Bottom) Separation of specimens using clustering (SOM) with the pore features "number of pores" and "pore density", with specimen-class distribution C:18, B:22, A:10 specimens (D class not included).

4.2 Scanned Immersion UT

After the experimental measurements with test frequencies of 25 and 50 MHz, it was decided to test the samples with a focusing probe with a frequency of 50 MHz and a focus at 50 mm in water. By a measured sound velocity of the samples of 6.9 mm / µs and a desired focal position of 1.5mm (material center) in the material, a calculated water flow of 43 mm was set. For the test area, the full width and the length between the "ejection points" were selected, with a resolution in the scan and index direction of 0.1 mm resolution.

The tests were carried out under the same reinforcement tested from both sides. Due to the sometimes strong curvature of the samples, a slight displacement of the diaphragms was partly necessary so that the A-image (entrance echo -EE- as trigger or the rear wall echo -RW-) does not run out of the diaphragm area too often and thus cannot be measured. For some samples, the curvature or the surface condition (grinding marks) was too large and lead to measurement value failure (white areas).

The C-images (largest amplitude in the aperture) of the volume and the RW are shown. Furthermore, a complete volume scan (A-images at each measuring position) is available. The 2-D representation could only represent the color-coded A-images of a scan line as an "expression", therefore the representation has been om-

itted. A visual comparison of the C images reveals differences between the class A-D samples. Apart from the increasing number of defects (A = > D), an ever-increasing noise, which leads to a reduction in the back-wall echo, can also be detected. In addition, a different number of ads can be seen between the samples "prim, sek-89, sek-58" of the respective "class", which always increases in each "class" from "prim" to "sek-58" to "sek-89". The samples can be recognized between "Class" A-D but also in the respective "Class" between "prim, sek-58 and sek-89".

Fig. 9 shows two examples comparing X-ray pore analysis and immersion UT scans (volume and back-wall). These two examples show a low correlation between the material-density-based X-ray analysis and the Ultrasonic wave-based immersion UT technique. Fig. 10 shows a comparison of the immersion scans for all four porosity classes. Although, the noise increases with increasing porosity, there is no direct quantitative measure of porosity and identification of single pores. There are dark areas in all scans not detectable via X-ray analysis, indicating non density-based defect.

Actually, one expects that the shading of the rear wall is simultaneously reflected as an amplitude increase in the area of the volume, as can be seen in "Probe Class B 031 prim side B". However, it could be that the pores, due to their surface curvature and small size, do not reflect the ultrasound back into the probe, but scatter it. That would explain why the back wall is shaded, but nothing is visible from the volume. What is otherwise visible from the volume and not in the X-ray could be scattering and grain boundaries. These reflect ultrasound, but do not lead to a change in optical density and are invisible in the X-ray.

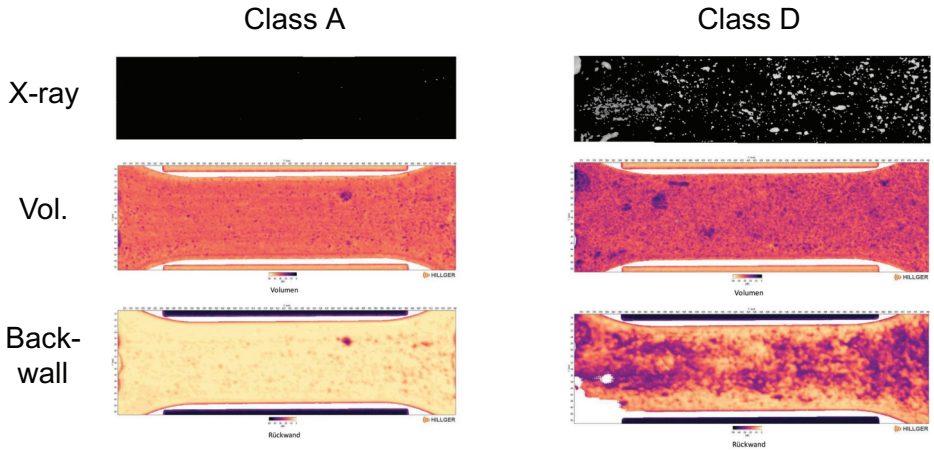

Fig. 9. Comparison of X-ray pore analysis and immersion UT scans.

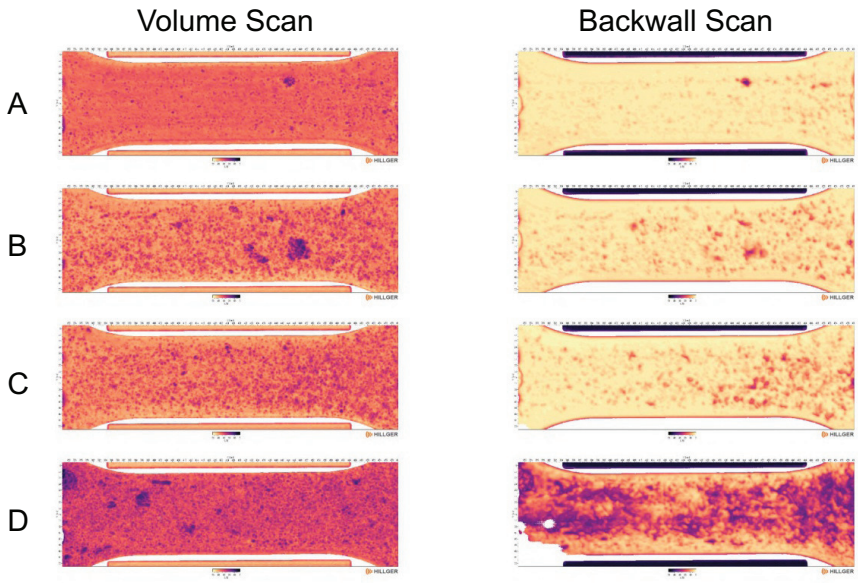

Fig. 10. Comparison of volume and back-wall immersion UT scans for different porosity classes (A: best, D: worst).

4.3 Pulse-Echo Ultrasonic

The dual-crystal Piezo transducer has a total contact diameter of 10 mm and typical main resonance frequency of about 5 MHz. In addition to the main resonance frequency there a side frequencies, each with a fwhm ~ 0.5 MHz:

- 6.3 MHz
- 5.3 MHz (main)
- 4.8 MHz
- 4.3 MHz
- 3.3 MHz
- 2.3 MHz

Five measurements along the long plate axis were performed. The sending coil was driven by a bipolar pulse of 100 ns duration and about 20 V_{pp} amplitude. The accumulative frequency spectra of the pulse-echo signals for different alloy and porosity classes are shown in Fig. 11. we found that the peak signal ratios for two different frequencies (5.3/4.3 MHz and peaks 5.3/6.3 MHz) were leading features to distinguish the alloy composition, as shown in Fig. 12.

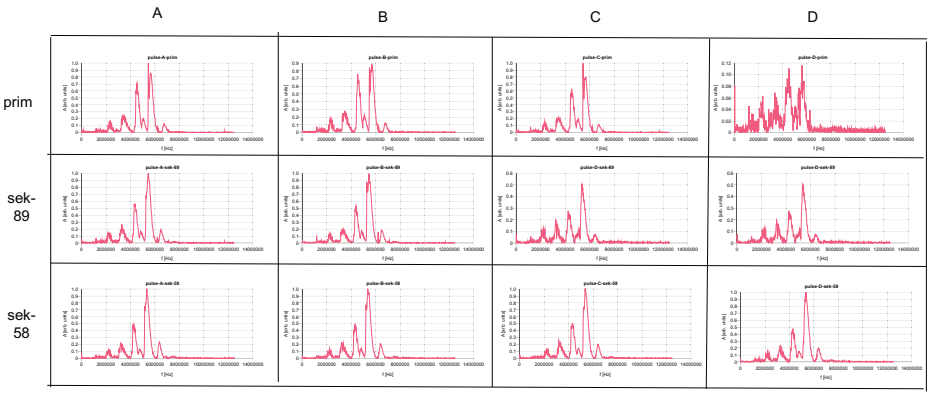

Fig. 11. Accumulative frequency spectra of pulse-echo signal response for different alloy and coarse porosity classes (A: best, D: worsest). There are six discrete peaks (inherent resonance frequencies of piezo transducers). Bipolar pulse duration is 100 ns. Main peak is at f=5.3 MHz, side peaks shifted by 1 MHz.

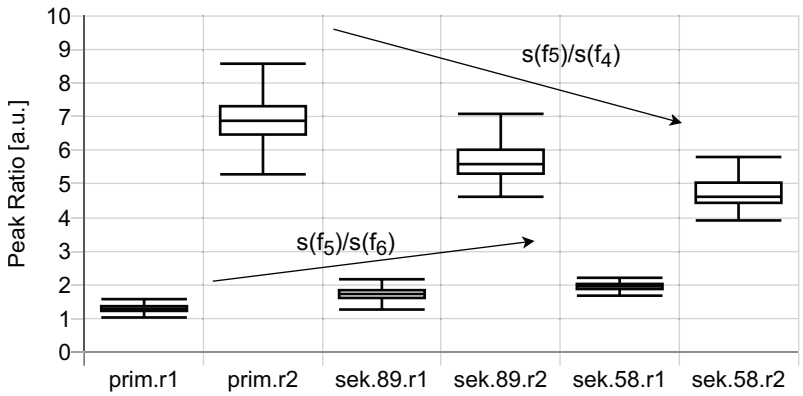

Fig. 12. Frequency ratios (signal peaks frq. 5.3/4.3 MHz and peaks freq. 5.3/6.3 MHz, Gaussian fitted) for different alloy classes

Alg. 1 shows a simple C50 decision trees using the two leading signal ratios $r_{5.3,4.3\ \mathrm{MHz}}$ and $r_{5.3,6.3\ \mathrm{MHz}}$ as the input attributes and the alloy class as the target attribute. The tree has a low height of 2 (3 nodes) with an acceptable classification error (14%). identification of the alloy class based on the signal frequency spectrum is possible. But the main goal of this study is the classification of the porosity based on the frequency spectrum, under the assumption that pores interact with the Us waves resulting in a frequency-dependent attenuation of the signal. The first issue is the nonuniform pore distribution in samples, as shown in Sec. 4.1.

```
Decision Tree
-------------

r5.4 <= 1.536585: prim (77/5)
r5.4 > 1.536585:
:...r5.4 <= 1.826923: sek-89 (48/8)
    r5.4 > 1.826923:
    :...r5.6 <= 4.75: sek-58 (9/1)
        r5.6 > 4.75 : sek-89 (28/9)

Evaluation (162 cases)
----------------------------------------

  Nodes     Errors
     3   23(14.2%)   <<
   (a)    (b)    (c)     <-classified as
  ----  ----  ----
    72      5           (a): class prim
     5     59      1     (b): class sek-89
           12      8     (c): class sek-58
Attribute usage:
    100%  r5.4
     23%  r5.6
```

Alg. 1. C50 decision tree for alloy classification based on the attributes r5.4 and r5.6 with confusion matrix (162 samples, no tree pruning and winnowing)

Using the frequency ratio features as an input for a decision classifying the porosity (based on the clustered classes A, B, C, and D) creates a significant larger tree with about 20 nodes. The classification error is below 20 % (guess probability for a class is 25 %), as shown in Alg. 2 A, but any further tests show a low generalization degree. It can be observed that the model classifies class B often as class A, which is an indicator of a weak discrimination between these two classes. Better results can be achieved with additional ratio attributes, as shown in Alg. 2 B, with lower prediction error and fewer tree nodes. Another observation is that if the original class labeling based on visual inspection is used, the classification error and tree size increases significantly, indicating a mislabeling by hand.

```
Model A. Evaluation (162 cases):
----------------------------------------

  Nodes      Errors
    21   29(17.9%)   <<
   (a)    (b)    (c)    (d)     <-classified as
  ----  ----  ----  ----
    55     15                  (a): class B
     2     69      1          (b): class A
     2      1      6      1    (c): class D
     3      4             3    (d): class C
Attribute usage:
    100%  r5.4
    100%  r5.6
Model B. Evaluation (154 cases):
----------------------------------------
```

```
    Decision Tree
  ----------------
  Size      Errors
    19   23(14.9%)   <<
   (a)    (b)    (c)    (d)    <-classified as
  ----  ----  ----  ----
    60     6           1    (a): class B
     7    59           1    (b): class A
     1          7     2    (c): class D
     2     3           5    (d): class C
Attribute usage:
    100%  r5.3
    100%  r5.4
     81%  r5.6
```

Alg. 2. C50 decision tree for porosity classification with confusion matrix (no tree pruning and winnowing). The class labeling was created with the unsupervised SOM clustering. A: Attributes r5.4 and r5.6, B: Attributes r5.3, r5.4, and r5.6.

5. Discussion and Conclusion

The entire work lacks ground-truth data and bases on experimental investigation. We investigated three different measuring methods to assess the porosity of HPDC aluminum plates. The primary method is pulse-echo UT with a low cost dual crystal transducer. The secondary methods used only to collect reference data are immersion scan UT and X-ray radioscopy. Pores are the primary detectable defect, which should be measured spatially resolved by the secondary methods and locally averaged by the primary method. The analysis of the X-ray images uses two methods, model-based classical image processing, and data-driven ML models. Pores show a low contrast in X-ray images, which require an accurate background intensity correction if a feature binarization is performed with a global threshold. We tested a naive approach using the mean intensity of the entire (corrected) image and increasing the mean value by a constant small factor (3%), and the Otsu and triangular methods. The mean offset approach outperformed the established otsu and triangular threshold approaches, which mostly failed entirely (no or all pixel marking). The pore feature marking of the constant offset method conforms with earlier die casting and material flow simulations, gaining enough trust to be used as reference data. The ML-based CNN approach used for automated feature marking failed here fully, in contrast to earlier work in [4], although trained with synthetic device-independent data from X-ray simulation. Here we used a different X-ray device with higher resolution, higher noise, but less contrast.

The results from the immersion scan UT show no conformance with the X-ray analysis with respect to pore detection. We can conclude that X-ray analysis is still the preferred method to assess and characterize porosity in aluminum materials. The specimens were classified in four porosity grades A-D, initially by visual inspection. Using selected statistical porosity measures from X-ray analysis (e.g., pore density and number of pores) as input data for an unsupervised ML clustering (Self-organizing Neuronal Maps) leads to a different classification compared with visual inspection, finally resulting in a classification difference of 43% of the specimens.

The spectral analysis of the pulse-echo UT signal data showed a strong correlation of the signal spectrum with the alloy distribution of the specimens (primary , secondary 58% and 89% materials). A simple decision tree (trained with C50 algorithm) requiring only two feature variables (two frequency peak ratios) and only three nodes was able to detect the alloy class with a classification error of about 10%.

But the correlation of the signal spectrum with the variation of the alloy composition must rely on a secondary effect, because the alloy variation is too small to have a significant impact on wave propagation. We guess that thin oxide films within the plate cause the shift of the frequency spectrum. The immersion scans show a first hint and difference in scans for the same porosity class, but different allay compositions.

The initial goal to classify the porosity class by the frequency spectrum showed average results. Although, a ML model like an Artificial Neural Network (ANN) or a decision tree can be used to map the frequency spectrum to our chosen porosity classes with reasonable accuracy, these models show a very low level of generalization and can be useless for real-word assessment of porosity with unknown specimens. Using frequency ratio features for classifying porosity results in a large decision tree with about 20 nodes and a classification error under 20%. However, the model struggles to distinguish classes B and A accurately, leading to misclassification. Improved outcomes can be obtained by incorporating additional ratio attributes, which reduce prediction error and tree size. Furthermore, relying on original class labels based on visual inspection significantly increases both classification error and tree size, suggesting issues with manual labeling.

6. References

[1] Cinkilic, E.; Moodispaw, M.; Zhang, J.; Miao, J.; Luo, A. A. A New Recycled Al-Si-Mg Alloy for Sustainable Structural Die Casting Applications. Metallurgical and Materials Transactions A 2022, 53A, 2861-2873, doi:10.1007/s11661-022-06711-4.

[2] Nunes, H.; Emadinia, O.; Soares, R.; Vieira, M. F.; Reis, A. Adding Valuer to Secondary Aluminum Casting Alloys: A Review on Trends and Achievements. Materials 2023, 16(3), 895, doi:10.3390/ma16030895.

[3] Balasubramani, N.; Moodispaw, M.; Luo, A. A. Controlling the Fe-intermetallic phases and mechanical properties of secondary Al-9Si-1Fe alloy with Cr and Mn additions. Journal of Materials Science & Technology 2025, 206, 135-152.

[4] Bosse, S., Lehmhus, D., Kumar, S., Automated Porosity Characterization for Aluminum Die Casting Materials Using X-ray Radiography, Synthetic X-ray Data Augmentation by Simulation, and Machine Learning, Sensors 2024, 24, 2933. https://doi.org/10.3390/s24092933

[5] Wilczek, Aneta, Piotr Długosz, and Marek Hebda: Porosity characterization of aluminium castings by using particular non-destructive techniques. Journal of Nondestructive Evaluation 34.3 (2015): 26.

[6] Boichuk, A. S., Dikov, I. A., Chertishchev, V. Y., & Generalov, A. S. (2019). Determining porosity of monolithic zones in aircraft parts and as-

semblies made of PCMs using ultrasound pulse echo method. Russian Journal of Nondestructive Testing, 55(1), 1-7.

[7] Hillger, W., Elze, S., DETERMINATION OF POROSITY IN AEROSPACE STRUCTURES BY ULTRASONIC PULSE ECHO TECHNIQUE, in 8th ECNDT, Barcelona, 2002.

[8] Adler, L., Wang, S.-W., Ultrasonic measurement of porosity in casts and welds. NASA. Lewis Research Center Analytical Ultrasonics in Materials Research and Testing, 1986.

[9] Gubernatis, Attenuation of Elastic Waves: J.E. and Domany, E., Effects of Microstructure on the Speed and Some Results for Porous Materials, in Review of Progress in Quantitative Nondestructive Evaluation (1983), ed. by D.O. Thompson and D.E. Chimenti.

[10] Rose, J. H., Ultrasonic Characterization of Porosity: Theory, to be published in Review of Progress in Quantitative Nondestructive Evaluation 1984.

7. Appendix

Alg. 3. Pseudo code of the pore analysis using X-ray images

```
1:  function PreProcessImage(image)
2:    // user selected ROI bounding  box or autocrop
3:    roi = select()
4:     // cropped image
5:    image.cropped = crop(image,roi)
6:    // integral vector of intensity
7:    profile.h = profile(image.cropped,axis=Horizontal)
8:    // integral vector of intensity
9:    profile.v = profile(image.cropped,axis=Vertical)
10:   // smoothing by polyfit, returns function
11:   profile.h.f = polyfit(profile.h,degree=4)
12:   profile.v.f = polyfit(profile.v,degree=4)
13:   // smoothed profile vectors
14:   profile.h' = profile.h.f(1:ncol(image.cropped))
15:   profile.v' = profile.v.f(1:nrow(image.cropped))
16:   // homogenize image intensity with h/v profile vectors
17:   image.cropped.homo = normalize(image.cropped,profile.h',profile.v')
18:   return image.cropped.homo
19: end
20: image.homo  = PreProcessImage(image)
21: // different thresholdsfor image binarization
22: image.cthr  = mean(image.homo)*1.03
23: image.otsu  = otsu(image.homo)
24: image.tria  = triangle(image.homo)
25: // binarize by threshold
26: image.feat  = image.homo >= image.cthr
```

```
// coordinate list
image.pts    = points(image.feat,threshold=0.5)
// cluster points to pore groups
image.clust = dbscan(image.pts,epsilon=3,minPts=10)
// compute pore hulls
image.hulls = { hull(pts), for each pts in image.clust }
pores.area  = { area(pts), for each hull pts in image.hulls }
pores.size  = { sqrt(area), for each area in pores.area }
...
```

Alg. 4. Pseudo code for finding relevant peaks in the frequency spectrum with Gaussian function fitting. x is a vector of frequencies, and y is a vector of amplitudes. An initial guess for the peak width must be provided.

```
function gaussfit(x,y,thr)
  y.norm = y/max(y)
  // convert y-axis to a log scale
  z = log(y.norm)
  // fit a parabola (quadratic) to the data
  (a,b,c) = polyfit(x,z,2)
  // calculate position, height and width of the Gaussian form,
  // from three coefficients of quadratic fit a,b,c
  height = exp(a-(c * pow(b/(2*c),2)))
  position = -b/(2*c);
  width = 2.35482/(sqrt(2)*sqrt(-c))
  return [height,position,width]
end
function smooth(N,y,smoothWidth)
  halfw = smoothWidth/2
  for i = 1 to N do
    s := []
    sumpoints := Σy[1:smoothWidth]
    for k = 1 to |y|-smoothWidth do
      s[k+halfw-1] := sumpoints
      sumpoints := sumpoints - y[k]
      sumpoints := sumpoints + y[k+smoothWidth]
    end
    y := s/smoothWidth
  end
  return y
end
function findPeaks(x,y,minFreq,maxFreq,initiaPeaklWidth)
  z  := smooth(3,y,SmoothWidth) // N=3: Approx. Gauss. filter
  d1 := deriv(z)
  d2 := deriv(d1)
  peaks := []
  // limited search range
  i1 = (i, x[i] >= minFreq)
  i2 = (i, x[i] <= maxFreq)
  // first guess of peak width in index units
  w  = initiaPeaklWidth/(x[2]-x[1])
  hw = w/2
```

```
39:   for i = i1 to i2 do
40:     if -d2[i] > thres and d[i]<0 and d[i-1]>0 then
41:      fit = gaussfit(x[(i-hw):(i+hw)],y[(i-hw):(i+hw)],0.01)
42:      peaks := peaks @
43:        {x=x[i],y=y[i],xg=fit[1],yg=fit[2],wg=fit[3]}
44:     end
45:   end
46:   return peaks
47: end
```